Response Times of Degenerately Doped Semiconductor Based Plasmonic Modulator

Raj Vinnakota (rvinnakota@troy.edu)
Troy University
Zuoming Dong
University of Texas Austin
Andrew Briggs
University of Texas Austin
Seth Banks
University of Texas Austin
Daniel Wasserman
University of Texas Austin
Dentcho Genov
Louisiana Tech University

Research Article

Keywords: Optoelectronics, Plasmonics, Surface Plasmon Polariton, PN Junction

Posted Date: August 22nd, 2022

DOI: https://doi.org/10.21203/rs.3.rs-1933673/v1

Response Times of Degenerately Doped Semiconductor Based Plasmonic Modulator

Raj K. Vinnakota[1*], Zuoming Dong[3], Andrew F. Briggs[3], Seth R. Bank[3], Daniel Wasserman[3] and Dentcho A. Genov[2]

[1*] Department of Chemistry and Physics, Troy University, Troy, AL 36082 USA

[2] College of Engineering and Science, Louisiana Tech University, Ruston, LA 71272 USA

[3] Department of Electrical and Computer Engineering, University of Texas Austin, Austin, TX 78758, USA

[*] *Corresponding author: rvinnakota@troy.edu; rajk.vinnakota@gmail.com*

Abstract: We present a transient response study of a semiconductor-based plasmonic switch. The proposed device operates through active control and modulation of localized electron density waves i.e., Surface Plasmon Polaritons (SPPs) at degenerately doped $In_{0.53}Ga_{0.47}As$ based PN^{++} junctions. A set of devices are designed and fabricated, and their optical and electronic behaviors are studied both experimentally and theoretically. Optical characterization shows far-field reflectivity modulation, a result of electrical tuning of the SPPs at the PN^{++} junctions for mid-IR wavelengths with significant 3dB bandwidths. Numerical studies using a self-consistent electro-optic multi-physics model are performed to uncover the temporal response of the devices' electromagnetic and kinetic mechanisms facilitating the SPP switching at the PN^{++} junctions. The numerical simulations show strong synergy with the experimental results, validating the claim of possible electrical tunability of the device with a 3dB bandwidth as high as 2GHz. Thus, this study confirms that the presented SPPD architecture can be implemented for high-speed control of SPPs through electrical means, potentially providing a pathway toward fast all-semiconductor plasmonic devices.

Keywords: Optoelectronics, Plasmonics, Surface Plasmon Polariton, PN Junction

Introduction:

To realize nanoscale integrated opto-electronic logic circuits, subwavelength confinement of light and integration of photonic devices with nanoscale electronics are indispensable [1-6]. In this context, the field of plasmonics opens a wide range of possibilities to design subwavelength, high speed, and high efficiency optical devices [7-20]. It is now well recognized by the research community that plasmonics provides possible solutions for integration between nano scale electronic and photonic components on a single chip, paving a new path toward optoelectronic devices characterized by fast information transfer and data processing [21-23]. Such capabilities can be accomplished through the excitation of Surface Plasmon Polaritons (SPPs), a collective excitation of electrons occurring at the interface between a metal/doped semiconductor and a dielectric medium [24]. Most importantly, the SPPs' exceptional spatial confinement at the metal-dielectric interface suggests them as one of the ideal candidates for the prospect of nanoscale chip level interconnects with spatial dimensions compatible with that of nanosized electronic devices.

Over the last few decades, due to advances in electromagnetic simulations and nanofabrication techniques, SPPs have attracted researchers resulting in a surge of progress towards promising applications such as super lenses [25, 26], light harvesting [27–28], metamaterials [29-32], plasmonic enhanced optoelectronics devices [33-38], and waveguiding and switching of SPPs [39-53]. In the context of plasmonic-based optoelectronic elements, so far, it has been showed that SPPs can be modulated at rates from a few kHz [54] to tens of MHz [43–45] and into the GHz range [55, 56]. Here, most of the reported works on SPP modulation use metal-dielectric structures. Metal-based optoelectronic devices can be applied toward integrated optical circuits if the device can successfully address the following challenges. First, common metals such as gold or silver have plasma frequency in the blue or deep ultra-violate wavelength ranges. There

are no available metals whose plasmon resonances are in the near or mid-infrared (MIR) wavelength range which is a highly useful wavelength range for detection and sensing applications [57, 58]. Second, large losses associated with metals stands as a key problem hindering the widespread implementation of metal-based architectures for many plasmonic and metamaterial applications. In addition, the plasma frequency for a given metal is fixed. Thus, there is no notable tunability offered by metal-dielectric structures that could benefit a variety of applications. New exciting physics behavior and applications of SPP based devices can arise if the dissipative losses in the metal-based plasmonic structures are reduced and a pathway toward integration with the current semiconductor technology is provided [59]. Such capabilities can be achieved if plasmonic devices are built based on highly doped semiconductors instead of conventional metals such as gold and silver. This is because heavily doped semiconductors can exhibit a small negative permittivity, low loss, and the potential for integration with semiconductor based electronic and optoelectronic devices [60-61]. It is also worth mentioning that while the field of metal based plasmonics is currently a mature discipline, the area of semiconductor based plasmonics is still rapidly developing.

In this work, we present a significant step towards realizing a complete semiconductor-based plasmonic switch referred to as a Surface Plasmon Polariton Diode (SPPD) [62-65]. Here, we build upon our past work [65], where we have demonstrated excitation and modulation of SPPs modes at the interface of the degenerately doped lattice-matched Indium Gallium Arsenide ($In_{0.53}Ga_{0.47}As$) PN^{++} **-** junctions grown epitaxially on Indium Phosphide (InP) and proceed to the next important step by experimentally demonstrating the temporal response of the device. Small signal frequency response measurements are performed, clearly demonstrating frequency dependent optical modulation (switching) of SPP modes at the PN^{++} junction. Furthermore, to

explore the factors determining the modulation speed of the SPPD, we employ an electro-optic Multiphysics numerical model, which self-consistently solves the PN^{++} junctions drift-diffusion equations at finite temperature (Fermi-Dirac statistics). The developed model provides accurate simulations of the local charge carrier dynamics, changes in the PN^{++}- junction capacitance and electro-optical modulation of the local charge density waves as a function of applied input signal voltage and wavelength. The theoretically performed small signal analysis correlates well to our experimental data, attesting to the potential of the proposed device architecture as an excellent electro-optic plasmonic switch. Moreover, our time dependent studies validates that the presented device architecture is capable of operating at 3dB bandwidths of up to 40MHz and, by scaling down the device spatial dimensions, can reach response times as high as 2GHz.

The presented device in this work, an all-semiconductor plasmonic switch, uses an $In_{0.53}Ga_{0.47}As$ based PN^{++}- diode. The diode is structured as a heavily doped *P*- layer and degenerately doped N^{++}- layer grown on Indium Phosphide (InP) and with active drift-diffusion region formed between an anode (top grating electrode) and a cathode (bottom contact). A schematic of the device is shown in Figure 1. The state of the device is considered 'ON' under zero external bias. The device architecture depicts a scenario of a "metal"-dielectric interface, where the heavily doped *P*- layer acts as a dielectric and the degenerately doped N^{++}- layer acts as a metal, thus supporting excitation of SPP modes at the PN^{++}- interface. To excite the SPP modes we use a grating coupling technique; where transverse magnetic (TM) polarized radiation is coupled to the SPPs at the interface via a grating. Under the presence of sufficient external forward bias voltage V, the charge carriers in N^{++}- doped layer gain enough energy to surpass the potential barrier provided by the PN^{++}- depletion region and are injected into the *P*- doped region. This charge injection process results in modifying the *P*-layer's permittivity ϵ_p. When applying external

bias $V > V_c$, where V_c is a critical voltage [65], some portion of the *P*-layer can acquire metal-like characteristics with $\epsilon_p < 0$, which results in hindering the propagation of the SPP modes within the active drift-diffusion region. This state of the device is considered as the 'OFF' state.

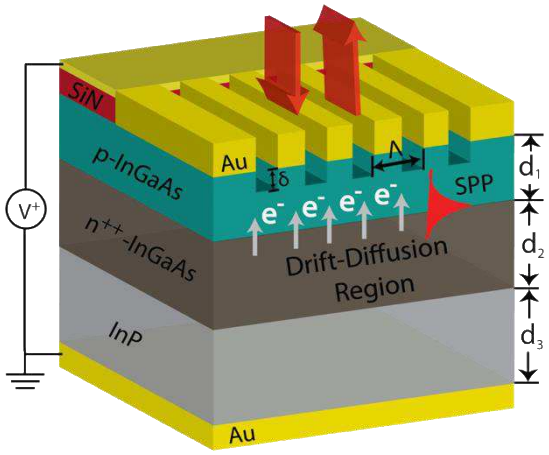

Figure 1 Basic architecture of Surface Plasmon Polariton Diode (SPPD), consisting of lattice matched Indium Gallium Arsenide ($In_{0.53}Ga_{0.47}As$) *PN*$^{++}$-junction grown epitaxially on an Indium Phosphide (InP) substrate. A grating with period $\Lambda = 2.4\ \mu m$ and *P*-layer etch depth of $\delta = 260nm$ are used to couple infrared incident light to the SPP modes to the *PN*$^{++}$-junction. The relevant device sizes are as follows; $d_1 = 0.75\ \mu m$, $d_2 = 1\ \mu m$, $d_3 = 500\ \mu m$.

The SPPD is fabricated from an epitaxially-grown Indium Gallium Arsenide ($In_{0.53}Ga_{0.47}As$) *PN*$^{++}$ junction lattice-matched to an Indium Phosphide (InP) substrate, with doping concentrations $N_D = 3.4 \times 10^{19} cm^{-3}$ and $N_A = 1 \times 10^{18} cm^{-3}$, respectively. The device fabrication process flow is shown in Figure 2. The fabrication begins with the metallization (Ti/Au, 10/500 nm) of the backside of a wafer to form the bottom electrode. A 640 nm silicon nitride layer was next deposited on the device top surface using plasma enhanced chemical vapor deposition (PECVD, $NH_3/N_2/SiH_4$, 10/500/40 sccm). The silicon nitride layer was then patterned into mesas

($700\mu m \times 600\mu m$) by UV lithography and dry etching using an Oxford80 reactive ion etcher (RIE) (CHF_3/O_2, 20/4 sccm). The patterned silicon nitride serves as an etch mask for the device mesas formed by dry etching using an Oxford100 inductively coupled plasma (ICP) system ($Cl_2/CH_4/H_2$, 6/4/7 sccm). Mesas were etched to a depth of 1300nm. The silicon nitride residue was then cleaned by buffered oxide etch (BOE). A 350 nm PECVD-deposited silicon nitride layer is then patterned to serve as an electrical isolation pad ($280\mu m \times 600\mu m$) on the top of the mesa structures. The device top contact, comprising a bond pad above the silicon nitride isolation pad and a grating structure contacting the top surface is shown in insert of Figure 5A, which is fabricated by UV lithography, metal deposition (Ti/Au, 10/250 nm) and lift-off. Finally, we performed another ICP dry etch to form the grating structure (etching to a depth of 260 nm) in the top p-InGaAs, using the top grating contact as a hard mask. During the dry etch, the top Au contact was etched 120nm, with the remainder of the sample protected by photoresist, and later cleaned by oxygen plasma. The sample was then mounted on copper blocks with indium paste and the top contact was wire-bonded to a Pasternack PE4542 SMA connector with ground pins soldered to the same copper block, shown in insert of Figure 5A.

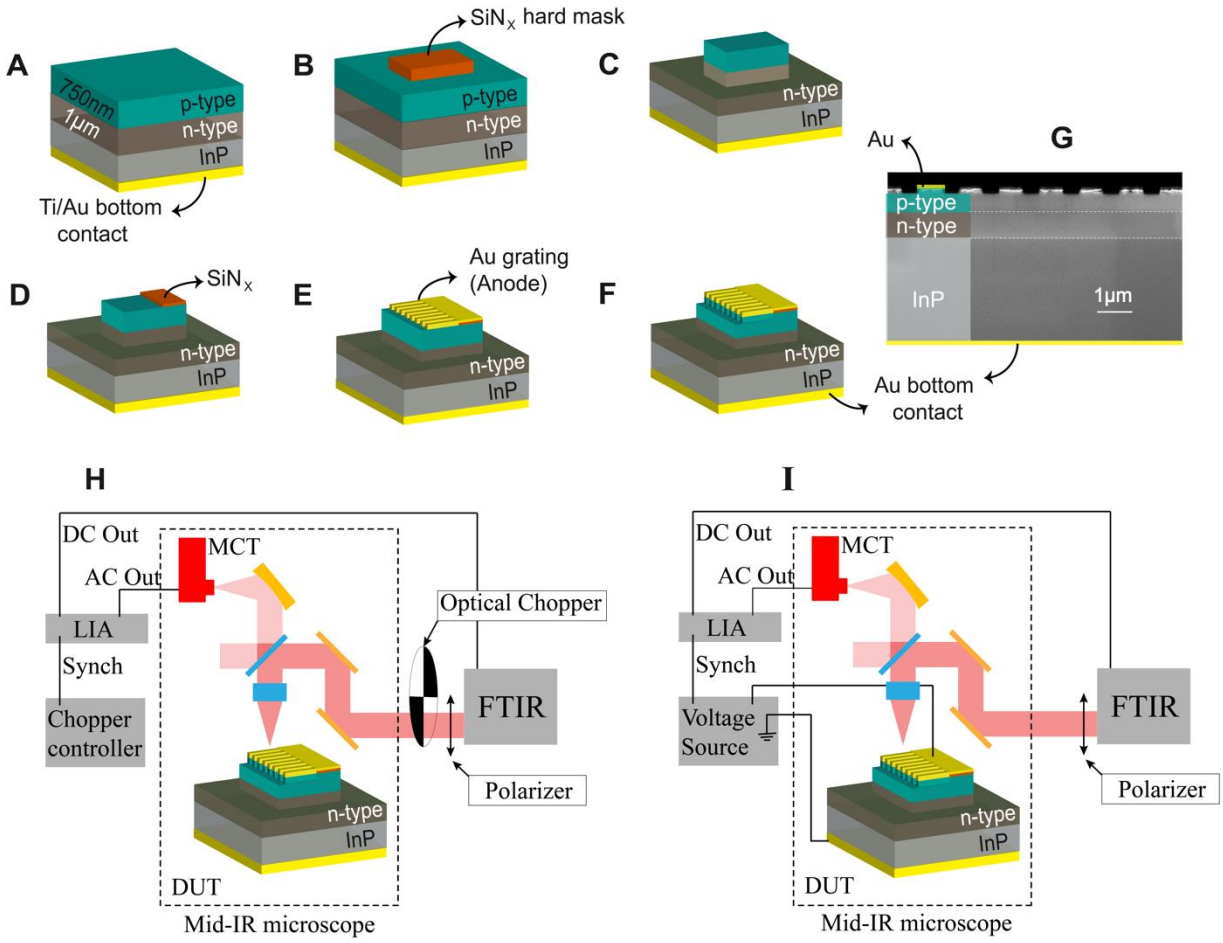

Figure 2 SPPD fabrication and experimental setup. (A) Layer structure of the $In_{0.53}Ga_{0.47}As$ PN^{++} diode grown on InP and bottom contact deposition. (B) Device layout after first SiN_x deposition and etch mask patterning (C) ICP dry etching to form the mesas on the *P*-doped layer, followed by a BOE etch to remove the SiN_x hard mask. (D) Second SiN_x deposition and patterning to provide an electrical isolation layer. (E) Top metal contact deposition. (F) ICP dry etch of the grating. Experimental set-up for polarization dependent reflectivity measurements under (G) zero voltage bias and (H) under external applied voltage modulation.

Following device fabrication, we performed polarization-dependent reflection spectroscopy using the setup shown in Figure 2H. Light from the internal source of a Bruker v80V Fourier transform infrared (FTIR) spectrometer was sent through a polarizer, modulated by a

mechanical optical chopper, and focused on the grating structures through a mid-IR microscope with a 15x Cassegrain objective. Reflected light was collected by the same objective and detected by the microscope's internal HgCdTe (MCT) detector. The output of the detector was sent to a lock-in amplifier synchronized to the optical chopper. The FTIR was operated in step scan mode, where at each mirror position, the output of the LIA was recorded, giving the interferogram of the reflected signal. The polarization-dependent reflectivity was then obtained by normalizing the sample reflection spectrum to the reflection from a gold surface measured in the same set-up. The transverse magnetic (TM) polarized reflectivity spectra of an unbiased device is shown in Figure 3A, with distinctive dips in reflectivity observed at $\lambda{\sim}7.3\mu m$ and $\lambda{\sim}11.4\mu m$. These reflection features correspond to coupling into electromagnetic (EM) modes supported either at the PN^{++}-interface or in the higher index P-layer of the device. To investigate these spectral features, we modified the already-developed COMSOL-based electro-optic model [62-65] to solve for the current device architecture and proceeded to numerically examine the fabricated SPPD. Essential parameters required to effectivity replicate the fabricated PN^{++}- junction such as doping concentrations at thermal equilibrium, junction depth, doping dependent and electron and hole mobilities and scattering rates, are used from our previous work [65]. The numerical model is designed to self-consistently solve for the device's position- and voltage-dependent charge carrier dynamics and the overall inhomogeneous local electron $n(\vec{r},V)$ and hole $p(\vec{r},V)$ concentration profiles, which are then used to calculate the inhomogeneous-, voltage-, and wavelength-dependent dielectric permittivity $\varepsilon(\vec{r},\omega,V)$ of the entire device which is used to study the device's electromagnetic response including the TM-polarized reflectivity [65].

The reflectivity spectra of the current device is depicted in Figure 3A. A very good correspondence between experiment and theory is observed, thus indicating the validity of the

model for the unbiased device. The field profiles associated with the observed reflectivity features at $\lambda{\sim}7.3\mu m$ and $\lambda{\sim}11.4\mu m$ are provided in Figure 3B and 3C. The calculated local energy density associated with the dip positioned at $\lambda{\sim}11.4\mu m$ in reflectivity spectra (see Figure 3B) clearly shows a localized profile located at the PN^{++} junction interface, suggesting the presence of a SPP mode. The mode profile related to the dip positioned at $\lambda{\sim}7.3\mu m$ in the reflectivity spectrum, (see Figure 3C) does not show the characteristic profile of an SPP, and instead can be attributed to typical Fabry-Perot resonances formed between the interface and the top surface.

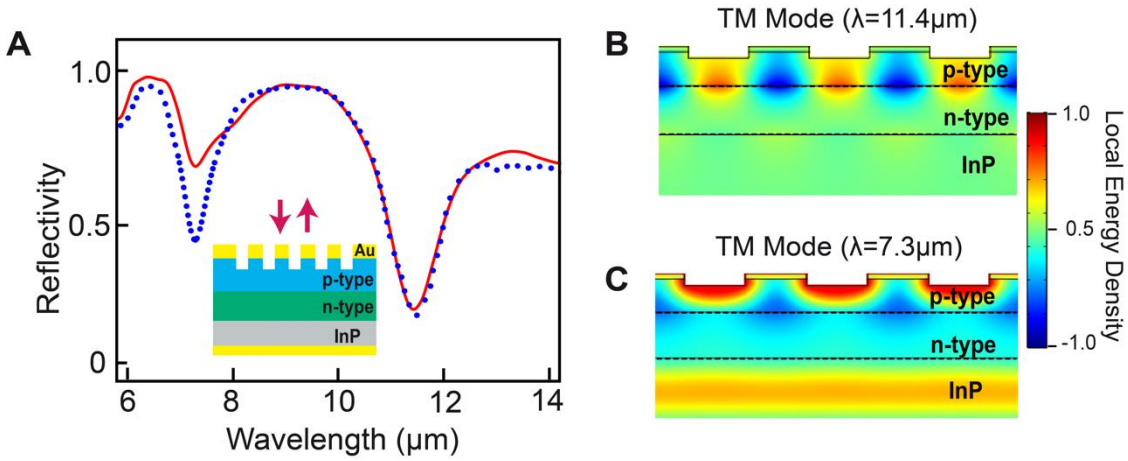

Figure 3 (A) Transverse magnetic (TM) polarized reflectivity spectra of the SPPD (see insert) under zero bias. The experimental data (solid line) is compared to self-consistent electro-optic simulations (dotted line). (B-C) The local energy densities across the device calculated at the wavelengths corresponding to the two dips in the reflectivity spectra, i.e., $\lambda = 11.4\mu m$ and $\lambda = 7.3\mu m$. The local energy density profiles clearly show the excitation of SPPs at the PN^{++}- junction for an incident wavelength of $\lambda = 11.4\mu m$.

To assess the device's steady state signal modulation, we have performed far field reflectivity studies both experimentally and numerically under four different forward voltages $V \in$

$\{660mV, 1060mV, 1200mV, 1260mV\}$. When evaluating the biased device's signal modulation experimentally, we used a setup similar to the one described for the unbiased device except that here the LIA is synchronized to a pulse generator which modulates the applied bias with a square wave at 10kHz and 50% Duty cycle. The interferogram generated in this experiment, when Fourier transformed, provides a measure of the modulation of the reflected signal as a function of wavelength. The modulation spectrum is then normalized to the sample's unbiased TM reflectivity, yielding the absolute change in reflectivity $\Delta R(\lambda)$ as a function of wavelength. The results are depicted in Figure 4, where we have plotted the absolute change in reflectivity $|\Delta R(\lambda, V)| = |R(\lambda, V) - R(\lambda, 0)|$, for added clarity focusing on the wavelength window centered on the SPP coupling wavelength ($\lambda = 11.4\,\mu m$). We clearly observe an increase in the far field reflectivity with an increase in the external forward bias. Such behavior can be attributed to the injection of a significant number of minority carriers into the device *P*-layer. Such increase in the local minority carrier concentration alters the *P*-layer's permittivity, eventually creating conditions that prohibit the excitation of SPP modes at the PN^{++} - junction, leading to the OFF state of the device at sufficiently large applied forward bias. These results validate our initial hypothesis, i.e., in presence of external forward voltage, injection of charge carriers into the *P*-layer will be sufficient to electrically modulate the coupled SPP modes at the PN^{++} - junction. We note that the observed far-field reflectivity modulation $\Delta R \approx 12\%$ of the presented device architecture is significantly higher compared to our previous studies [65], where a modest modulation of $\Delta R \approx 1\%$ was demonstrated. This can be attributed to the specific placement of the bottom electrodes in the new device. Specifically, in our previous studies [65] the bottom electrodes are placed on either side of the PN^{++} Layer, whereas in the current architecture the bottom electrode is deposited at the bottom of the InP layer. Thus, changing the position of the bottom electrode can result in reducing

the effect of current spreading, providing a channel for larger concentration of minority carriers to be injected into the P-Layer resulting in a larger change in the P-layer permittivity and consequently the far-field reflectivity.

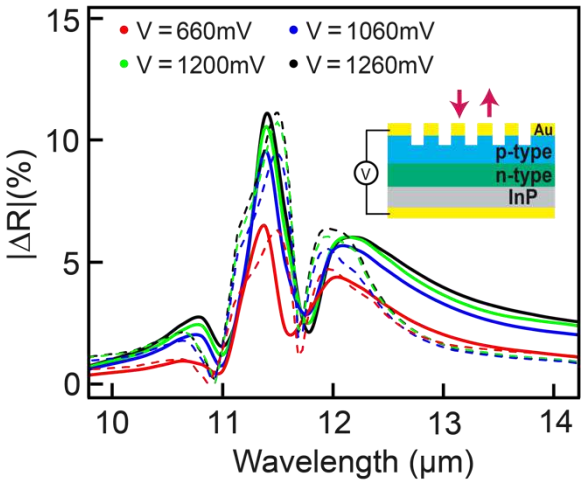

Figure 4 Steady state SPPD reflectivity modulation. The absolute change in reflectivity is experimentally obtained under various forward bias voltages (solid lines) and compared to the self-consistent electro-optic simulations (dashed lines).

To assess the SPPD 3dB bandwidth, we have performed small signal transient analysis of the device through reflectivity measurements at a fixed input wavelength. Here, we used a CO_2 laser as a Continuous Wave (CW) source, tuned to an emission wavelength of $\lambda = 10.61\ \mu m$, roughly corresponding to the short wavelength side of the feature, which will decrease the amplitude of modulation, but should not affect the achievable frequency of modulation (see Figure 4). The light from the laser was sent through a beam splitter with reflected light measured by a power meter and used as reference for the source power, in order to normalize for fluctuations in the laser power over time. The light transmitted through the beam splitter is focused on the sample

through a ZnSe lens with a 2-inch focal length. The sample was modulated by the output of a Zurich UHF lock-in amplifier (LIA), which was programmed to output an AC (sine wave) signal with varying DC offset; $V_F = V_{dc} + V_{ac}\sin(\omega t)$ applied to the device. The amplitude of the applied voltage is limited by the series resistance (R_0), which is the sum of the internal resistance of the function generator and the transmission line impedance. For our setup and low frequencies, we observed $R_0 = 100\Omega$. The reflected light was collected by the same ZnSe lens, incident on the beam splitter, with the reflected signal detected by a Boston Electronics PVM-10.6 room-temperature MCT detector (time constant 1.5ns). The output of the detector was then fed into the Zurich LIA, synchronized to the device-driving AC signal (V_F). The complete setup is depicted in Figure 5A.

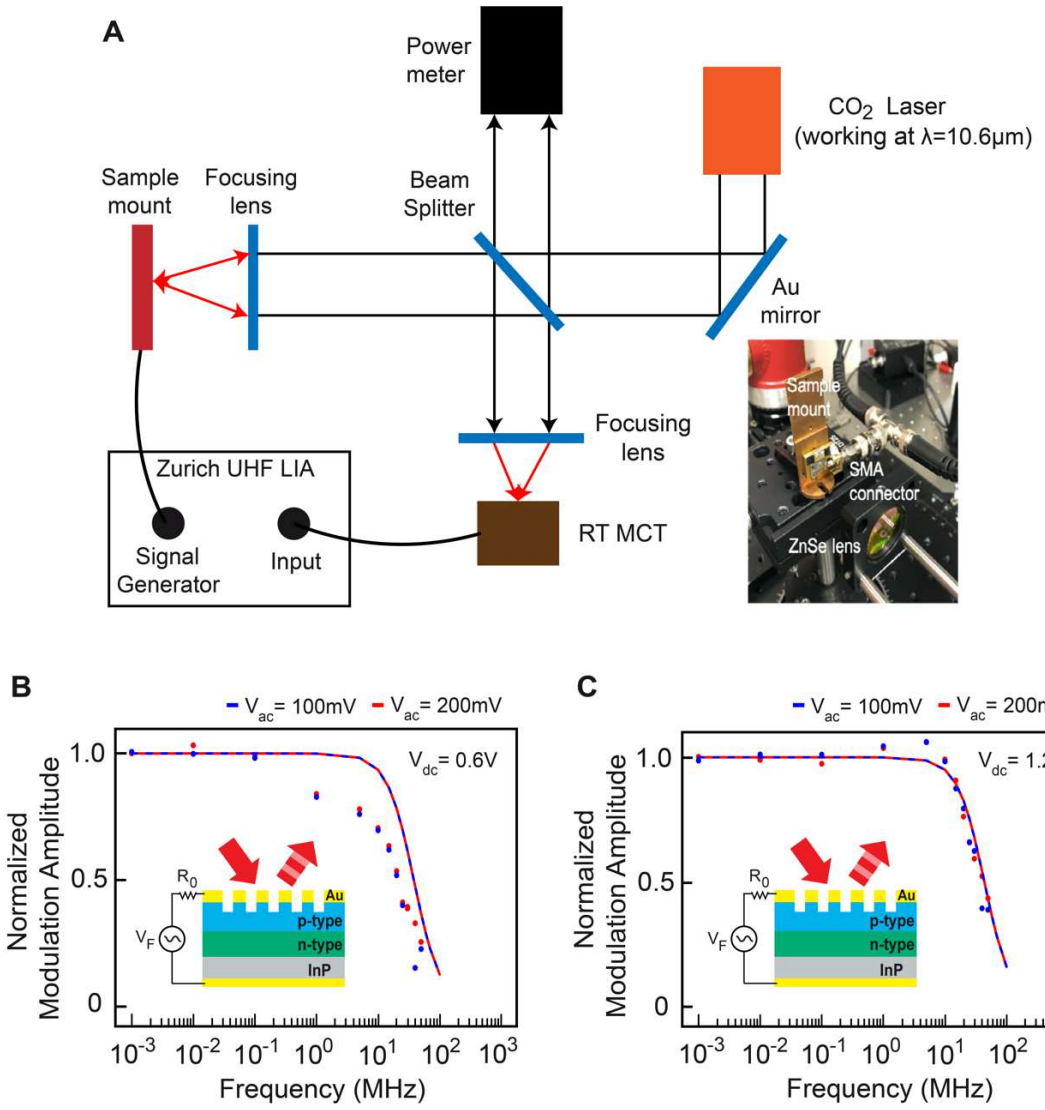

Figure 5 SPPD frequency response. (A) Experimental setup schematic. Normalized far field modulation as a function of input driving AC small signal frequency, obtained under two sets of low frequency sinusoidal signal: (B) $V_{dc} = 0.6V$ and $V_{ac} = (100mV, 200mV)$ (C) $V_{dc} = 1.2V$ and $V_{ac} = (100mV, 200mV)$. Experimental data is represented in dotted lines compared to the self-consistent electro-optic simulations (dashed lines). In the calculations the operation wavelength is set at $\lambda = 10.61\mu m$.

Figures 5B, and 5C depicts the experimentally measured frequency response of the device under four sets of sinusoidal input signals with driving frequencies varying from 1kHz up to 100MHz. The data indicates SPP modulation with 3dB bandwidths of 25MHz for DC voltage of 0.6V and 40MHz for DC voltage of 1.2V. The frequency response of the device is only weakly dependent on the small-signal AC voltage as expected. To explore the factors that determine the 3dB response of the device in higher details, we have compared the experimental data to numerical simulations (solid and dashed lines in Figure 5B and 5C). Overall, the theory agrees with the experimentally observed behavior both qualitative and quantitatively. We must note that the predicted and observed bandwidths are substantially lower compared to simulations performed by the authors elsewhere for shorter SPPDs [62, 63]. Indeed, this discrepancy is easily understood based on the fact that the fabricated device has a bottom InP layer with thickness $d_3 = d_{InP} = 500\ \mu m$ (see Figure 1) and doping concentration of $1 \times 10^{18} cm^{-3}$. From simulations we observe that this layer provides an estimated resistance of $R_{InP} \sim 79 m\Omega$ translating into an additional voltage drop across the layer of the order of $\Delta V_{InP} \sim 0.25V$ and additionally the time constant associated with the entire system that depends on the diffusion capacitance and differential resistance play a crucial role in the observed devices' reduced 3dB bandwidth. Hence, we expect that reducing the InP layer thickness should lead to substantial speed up of the SPPD switching speed.

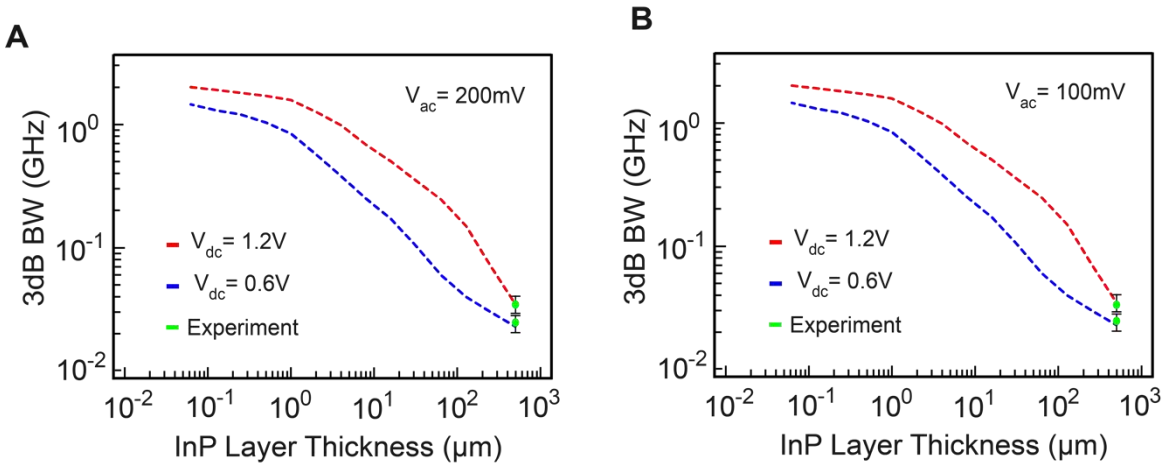

Figure 6 Numerical calculation of SPPD 3dB response times as function of the InP Layer thickness. In the calculations the device is operated using two sets of low frequency sinusoidal signal: (A) $V_{ac} = 200mV$ and $V_{dc} \in \{0.6V, 1.2V\}$ (B) $V_{ac} = 100mV$ and $V_{dc} \in \{0.6V, 1.2V\}$. Experimental data is depicted in green dots. In the calculations the operation wavelength is set at $\lambda = 10.61\mu m$.

To better assess the SPPD 3dB response as a function of InP layer thickness, we have proceeded to numerically characterize the fabricated $In_{0.53}Ga_{0.47}As$ based SPPD by theoretically decreasing the InP layer thickness. In the simulations we keep the same set of input voltages as those per Figure 5 and operated the device at the same incident wavelength of $\lambda = 10.61\mu m$. Our results are shown in Figure 6. As expected, the 3dB bandwidth is found to be inversely proportional with the InP thickness and then saturates for thin devices ($d_{InP} < 1\mu m$) at about 2GHz. This is because the electron injection rate into the *P*-layer is inversely proportional to d_{InP} and proportional to the applied voltage bias, indicating that the optical modulation cutoff frequency is limited by the circuit speed. This distinctive behavior can be quantitatively explained using a simple drift-diffusion model of the electron dynamics within the drift-diffusion region. Overall,

our data shows that for a bare device, without the InP layer, 3dB bandwidth in excess of 2GHz can be achieved. Further improvement in the device's response times is expected by reducing the size of the drift-diffusion region (and varying the P and N^{++}- layers doping concentrations while keeping the SPP operation frequency within the mid-IR spectral range. Such type of optimization studies will be subject of future work.

Conclusion

In conclusion we have performed time response analysis and optical characterization of an all-semiconductor based plasmonic switch, referred to as Surface Plasmon Polariton Diode (SPPD), comprising a grating-coupled, lattice-matched $In_{0.53}Ga_{0.47}As$ degenerate PN^{++}- junction. Following, electrical control and temporal modulation of Surface Plasmon Polaritons (SPPs) at degenerate semiconductor interface is demonstrated within the mid-IR frequency range. The 3dB response times and the far-field reflectivity under the presence of a small signal AC bias was extensively studied experimentally and compared to numerical simulations, validating the proposed switching mechanism underlying the SPPD operation. Our data shows that the presented device architecture with 500 μm InP layer can support 3dB bandwidths of 45MHz. Based on the excellent match between theory and experiment, we have performed small-signal transient studies of prospective SPPDs with various InP layer thickness. The data shows that the proposed SPPD architecture can provide 3dB bandwidths of up to 2GHz. Overall, the presented study indicates that degenerate semiconductor junctions can efficiently support excitation and control of SPP modes at mid-IR frequencies, an important step toward realization of prospective plasmonic circuit elements.

Funding and Acknowledgements:

RV and DG gratefully acknowledge funding from the National Science Foundation (Award No. ECCS-1610200) and National Science Foundation EPSCoR CIMM project (Award No. OIA-1541079). ZD and DW gratefully acknowledge funding from the National Science Foundation (Award No. ECCS-1611231). RV gratefully acknowledge funding from the National Science Foundation ERI (Award No. ECCS-2138198).

Author Contributions:

R. V., Z. D., D. W. and D. A. G. contributed equally to executing the idea, analyzing the data and writing the manuscript. S. B. and A. B. grew the material.

Competing Interests:

The authors declare that they have no competing interests.

Availability of Data and Materials:

All data included in this article are available from the corresponding author upon reasonable request.

Code Availability:

All codes included in this article are available from the corresponding author upon reasonable request.

References:

1. Hira T, Homma T, Uchiyama T, Kuwamura K, Kihara Y, Saiki T (2015) All-optical switching of localized surface plasmon resonance in single gold nanosandwich using GeSbTe film as an active medium. Appl Phys Lett 106:031105. https://doi.org/10.1063/1.4906037
2. Guo PJ, Schaller RD, Ketterson JB, Chang RPH (2016) Ultrafast switching of tunable infrared plasmons in indium tin oxide nanorod arrays with large absolute amplitude. Nature Photon 10:267–274. https://doi.org/10.1038/nphoton.2016.14
3. Kriegel I, Urso C, Viola D, De Trizio L, Scotognella F. Cerullo G et al (2016) Ultrafast photodoping and plasmon dynamics in fluorine–indium codoped cadmium oxide nanocrystals for all-optical signal manipulation at optical communication wavelengths. J Phys Chem Lett 7:3873– 3881. https://doi.org/10.1021/acs.jpclett.6b01904
4. Chai Z, Zhu Y, Hu XY, Yang X, Gong ZB, Wang FF et al (2016) On-chip optical switch based on plasmon–photon hybrid nanostructure-coated multicomponent nanocomposite. Adv Opt Mater 4:1159– 1166. https://doi.org/10.1002/adom.201600271
5. Nurmohammadi T, Abbasian K, Yadipour R (2018) Ultra-fast all-optical plasmonic switching in near infra-red spectrum using a Kerr nonlinear ring resonator. Opt Commun 410:142–147. https://doi.org/10.1016/j.optcom.2017.09.082
6. Baig SA, Boland JL, Damry DA, Tan HH, Jagadish C, Joyce HJ et al (2017) An ultrafast switchable terahertz polarization modulator based on III–V semiconductor nanowires. Nano Lett 17:2603-2610. https://doi.org/10.1021/acs.nanolett.7b00401
7. Zhang XP, He JF, Wang YM, Liu FF (2016) Terahertz beat oscillation of plasmonic electrons interacting with femtosecond light pulses. Sci Rep 6:18902. https://doi.org/10.1038/srep18902

8. McPolin CP, Olivier N, Bouillard JS, O'Connor D, Krasavin AV, Dickson W et al (2017) Universal switching of plasmonic signals using optical resonator modes. Light Sci Appl. 6:e16237. https://doi.org/10.1038/lsa.2016.237
9. Kumar N, Rúa A, Aldama J, Echeverria K, Fernández FE, Lysenko S (2018) Photoinduced surface plasmon switching at VO_2/Au interface. Opt Exp 26:13773–13782. https://doi.org/10.1364/OE.26.013773
10. Wang KD, Chen L, Zhang HJ, Chen J (2017) Controlling surface plasmon polaritons at femtosecond timescales on an aluminum-coated grating. Appl Phys Lett 110:021105. https://doi.org/10.1063/1.4973860
11. Vasa P, Wang W, Pomraenke R, Maiuri M, Manzoni C, Cerullo G et al (2015) Optical Stark effects in J-aggregate metal hybrid nanostructures exhibiting a strong exciton–surface-plasmon-polariton interaction. Phys Rev Lett 114:036802–036806. https://doi.org/10.1103/physrevlett.114.036802
12. Dai HW, Zhang LM, Wang ZW, Wang X, Zhang JP, Gong HM et al (2017) Linear and nonlinear optical properties of silver-coated gold nanorods. J Phys Chem C 121:12358–12364. https://doi.org/10.1021/acs.jpcc.7b00295
13. Wang H, Wang HY, Toma A, Yano TA, Chen QD, Xu HL et al (2016) Dynamics of strong coupling between CdSe quantum dots and surface plasmon polaritons in subwavelength hole array. J Phys Chem Lett 7:4648– 4654. https://doi.org/10.1021/acs.jpclett.6b02059
14. Kim J, Carnemolla EG, DeVault C, Shaltout AM, Faccio D, Shalaev VM et al (2018) Dynamic control of nanocavities with tunable metal oxides. Nano Lett 18:740–746. https://doi.org/10.1021/acs.nanolett.7b03919

15. Della Valle G, Polli D, Biagioni P, Martella C, Giordano MC, Finazzi M et al (2015) Self-organized plasmonic metasurfaces for all-optical modulation. Phys Rev B 91:235440. https://doi.org/10.1103/physrevb.91.235440

16. Sim S, Jang H, Koirala N, Brahlek M, Moon J, Sung JH et al (2015) Ultrahigh modulation depth exceeding 2,400% in optically controlled topological surface plasmons. Nat Commun 6:9814–9817. https://doi.org/10.1038/ncomms9814

17. Lu CC, Hu XY, Shi KB, Hu Q, Zhu R, Yang H, Gong QH (2015) An actively ultrafast tunable giant slow-light effect in ultrathin nonlinear metasurfaces. Light Sci Appl. 4:e302–e309. https://doi.org/10.1038/lsa.2015.75

18. Thomas A, Savaliya P, Kumar K, Ninawe A, Dhawan A (2018) Au nanowire-VO_2 spacer-Au film based optical switches. J.Opt.Soc.Am.B 35:1687–1697. https://doi.org/10.1364/JOSAB.35.001687

19. Zhang XP, Sun BQ, Hodgkiss JM, Friend RM (2008) Tunable ultrafast optical switching via waveguided gold nanowires. Adv Mater 20:4455–4459. https://doi.org/10.1002/adma.200801162

20. Sharma Y, Tiruveedhula VA, Muth JF, Dhawan A (2015) VO_2 based waveguide-mode plasmonic nano-gratings for optical switching. Opt Express 23:5822–5849. https://doi.org/10.1364/OE.23.005822

21. Zia, R, Schuller J A, Chandran A, Brongersma ML (2006) Plasmonics: the next chip-scale technology. Mater. Today 9:20–27. https://doi.org/10.1016/S1369-7021(06)71572-3

22. Maier S, Brongersma ML et al. (2003) Plasmonics – A Route to Nanoscale Optical Devices (Advanced Materials, 2001, 13, 1501). Adv. Mater 15:562–562. https://doi.org/10.1002/adma.200390134

23. Brongersma ML, Shalaev VM (2010) The Case for Plasmonics. Science 328:440–441. https://www.science.org/doi/10.1126/science.1186905

24. Pitarke JM, Silkin VM, Chulkov EV, Echenique PM (2007) Theory of surface plasmons and surface-plasmon polaritons. Rep. Prog. Phys 70: 1-87. https://doi.org/10.1088/0034-4885/70/1/r01

25. Pendry JB (2000) Negative refraction makes a perfect lens. Phys. Rev. Lett 85:3966–3969. https://doi.org/10.1103/physrevlett.85.3966

26. Zhang X, Liu Z (2008) Superlenses to overcome the diffraction limit. Nat. Mater 7: 435–441. https://doi.org/10.1038/nmat2141

27. Tian Y, Tatsuma T (2005) Mechanisms and applications of plasmon-induced charge separation at TiO2 films loaded with gold nanoparticles. J. Am. Chem. Soc 127:7632–7637. https://doi.org/10.1021/ja042192u.s001

28. Zeng P, Cadusch J et al (2016) Photoinduced electron transfer in the strong coupling regime: waveguide-plasmon polaritons. Nano Lett 16:2651–2656. https://doi.org/10.1021/acs.nanolett.6b00310

29. Hedayati MK, Javaherirahim M et al (2011) Design of a perfect black absorber at visible frequencies using plasmonic metamaterials. Adv. Mater 23:5410–5414. https://doi.org/10.1002/adma.201102646

30. Shalaev V (2007) Optical negative-index metamaterials. Nature Photon 1: 41–48. https://doi.org/10.1038/nphoton.2006.49

31. Valentine J, Zhang S et al (2008) Three-dimensional optical metamaterial with a negative refractive index. Nature 455:376–379. https://doi.org/10.1038/nature07247

32. Mundru PC, Pappakrishnan V, Genov DA (2012) Material- and geometry-independent multishell cloaking device. Phys. Rev. B - Condens. Matter Mater. Phys 85:045402. https://doi.org/10.1103/physrevb.85.045402
33. Sasaki K, Nagamura T (1998) Ultrafast wide range all-optical switch using complex refractive-index changes in a composite film of silver and polymer containing photochromic dye. J. Appl. Phys 83:2894-2900. https://doi.org/10.1063/1.367076
34. Macdonald KF, Krasavin AV, Zheludev NI (2007) Optical modulation of surface plasmon-polariton coupling in a gallium/ aluminium composite. Opt. Commun 278:207–210. https://doi.org/10.1016/j.optcom.2007.06.010
35. Zhang X, Sun B, Hodgkiss JM, Friend RH (2008) Tunable Ultrafast Optical Switching via Waveguided Gold Nanowires. Adv. Mater 20:4455–4459. https://doi.org/10.1002/adma.200801162
36. Dintinger J, Robel I, Kamat PV, Genet C, Ebbesen TW (2006) Terahertz All-Optical Molecule- Plasmon Modulation. Adv. Mater 18:1645–1648. https://doi.org/10.1002/adma.200600366
37. Wurtz GA, Pollard R, Zayats AV (2006) Optical Bistability in Nonlinear Surface-Plasmon Polaritonic Crystals. Phys. Rev. Lett 97:057402. https://doi.org/10.1103/physrevlett.97.057402
38. Nordin L, Petluru P, Kamboj A, Muhowski AJ, Wasserman D. (2021) Ultra-thin plasmonic detectors. Optica. 2021; 8: 1545. https://doi.org/10.1364/optica.438039
39. Abbas MN, Cheng CW, Chang YC, Shih MH (2012) An omni-directional mid-infrared tunable plasmonic polarization filter. Nanotechnology 23:444007. https://doi.org/10.1088/0957-4484/23/44/444007

40. Wang G, Lu H, Liu X, Gong Y (2012) Numerical investigation of all-optical switch in graded nonlinear plasmonic grating. Nanotechnology 23:444009. https://doi.org/10.1088/0957-4484/23/44/444009

41. Krasavin AV, Zayats AV (2010) Electro-optic switching element for dielectric-loaded surface plasmon polariton waveguides. Appl. Phys. Lett 97:041107. https://doi.org/10.1063/1.3464552

42. Chen J, Li Z, Zhang X, Xiao J, Gong Q (2013) Submicron bidirectional all-optical plasmonic switches. Sci. Rep 3:824–830. https://doi.org/10.1038/srep01451

43. Lereu AL, Passian A, Goudonnet JP, Thundat T, Ferrell TL (2005) Optical modulation processes in thin films based on thermal effects of surface plasmons. Appl. Phys. Lett 86:154101. https://doi.org/10.1063/1.1900311

44. Passian A, Lereu AL, Arakawa ET, Wig A, Thundat T, Ferrell TL (2005) Modulation of multiple photon energies by use of surface plasmons. Opt. Lett 30:41-43. https://doi.org/10.1364/ol.30.000041

45. Passian A, Lereu AL, Arakawa ET, Ritchie RH, Thundat T, Ferrell TL (2004) Opto-electronic versus electro-optic modulation. Appl. Phys. Lett 85:2703-2705. https://doi.org/10.1063/1.1804252

46. Nielsen MG, Bernardin T, Hassan K, Kriezis EE, Weeber JC. (2014) Silicon-loaded surface Plasmon polariton waveguides for nanosecond thermo-optical switching. Optics Letters 39:2282-2285. https://doi.org/10.1364/ol.39.002282

47. Yuan GH, Yuan XC, Zhang DG, Wang P, Ming H, Mei T (2009) Numerical demonstration of all-optical switching in dielectric-loaded surface Plasmon polaritonic crystal with a defect mode. J. Opt. A: Pure Appl. Opt 11:085005. https://doi.org/10.1088/1464-4258/11/8/085005

48. Krasavin AV, Zayats AV, Zheludev NI (2005) Active control of surface Plasmon-polariton waves. J. Opt. A: Pure Appl. Opt 7: S85-S89. https://doi.org/10.1088/1464-4258/7/2/011
49. Wu X, Li D, Sun WH, Peng RW (2009) Coupling of Terahertz Surface Plasmon Polaritons in Corrugated Stacks of Dielectric and Semiconductor. PIERS Online 5:101-104. https://doi.org/10.2529/piers080906050944
50. Sanchez-Gil JA, Rivas JG (2006) Thermal switching of the scattering co-efficient of terahertz surface Plasmon polaritons impinging on a finite array of subwavelength grooves on semiconductor surfaces. Phys. Rev. B 73:205410. https://doi.org/10.1103/physrevb.73.205410
51. Özdemir SK (2003) Temperature Effects on Surface Plasmon Resonance: Design Considerations for an Optical Temperature Sensor. IEEE Journal of Lightwave Technology 21:805-814. https://doi.org/10.1109/jlt.2003.809552
52. Yang T, Li XA, Huang W, Ho HP (2012) Thermal Switching of Terahertz Surface Plasmon Polaritons in Semiconductors. 17th Opto-Electronics and Communications Conference 703-704. https://doi.org/10.1109/oecc.2012.6276800
53. J. Gosciniak and S. I. Bozhevolnyi. (2013) Performance of thermo-optic components based on dielectric-loaded surface plasmon polariton waveguides. Sci Rep. 3:1803. https://doi.org/10.1038/srep01803
54. Pacifici D, Lezec H, Atwater H (2007) All-optical modulation by plasmonic excitation of CdSe quantum dots. Nature Photon 1:402–406. https://doi.org/10.1038/nphoton.2007.95
55. Haffner C, Heni W, Fedoryshyn Y et al (2015) All-plasmonic Mach–Zehnder modulator enabling optical high-speed communication at the microscale. Nature Photon 9**:**525–528. https://doi.org/10.1038/nphoton.2015.127

56. Ayata M et al. (2017) High-speed plasmonic modulator in a single metal layer. Science 358: 630–632. https://doi.org/10.1126/science.aan5953

57. Soref R (2010) Mid-infrared photonics in silicon and germanium. Nature Photon 4: 495–497. https://doi.org/10.1038/nphoton.2010.171

58. Soref R, Peale RE, Buchwald W (2018) Longwave plasmonics on doped silicon and silicides. Opt. Express 16:6507–6514. https://doi.org/10.1364/oe.16.006507

59. Brongersma ML, Zia R, Schuller J (2007) Plasmonics – the missing link between nanoelectronics and microphotonics. Applied Physics A 89:221–223. https://doi.org/10.1007/s00339-007-4151-1

60. Law S, Adams DC, Taylor AM, Wasserman D (2012) Mid-infrared designer metals. Optics Express 20**:**12155. https://doi.org/10.1109/ipcon.2012.6358858

61. Law S, Yu L, Wasserman D (2013) Epitaxial growth of engineered metals for mid-infrared plasmonics. J. Vac. Sci. Technol. B 31:03C121. https://doi.org/10.1116/1.4797487

62. Vinnakota RK, Genov DA (2014) Terahertz optoelectronics with surface plasmon polariton diode. Sci. Rep 4:4899. https://doi.org/10.1038/srep04899

63. Vinnakota RK, Genov DA (2017) Active Control of Charge Density Waves at Degenerate Semiconductor Interfaces. Sci. Rep 7:10778. https://doi.org/10.1038/s41598-017-11005-6

64. Dong Z, Vinnakota RK, Briggs AF, Nordin L, Bank SR, Genov DA, Wasserman D (2019) Electrical modulation of degenerate semiconductor plasmonic interfaces. Journal of Applied Physics 126:043101. https://doi.org/10.1063/1.5108905

65. Vinnakota RK, Dong Z, Briggs AF, Bank SR, Wasserman D, Genov DA (2020) Plasmonic electro-optic modulator based on degenerate semiconductor interfaces. Nanophotonics 9:1105-1113. https://doi.org/10.1515/nanoph-2019-0518